

Imaging of the CO snow line in a solar nebula analog

Chunhua Qi^{1*}, Karin I. Öberg^{2*}, David J. Wilner¹, Paola d’Alessio³,
Edwin Bergin⁴, Sean M. Andrews¹, Geoffrey A. Blake⁵,
Michiel R. Hogerheijde⁶, Ewine F. van Dishoeck^{6,7}

¹Harvard-Smithsonian Center for Astrophysics

²Departments of Chemistry and Astronomy, University of Virginia

³Centro de Radioastronomia y Astrofisica, Universidad Nacional Autonoma de Mexico

⁴Department of Astronomy, University of Michigan

⁵Division of Geological and Planetary Sciences, California Institute of Technology

⁶Leiden Observatory, Leiden University

⁷Max Planck Institute for Extraterrestrial Physics

*Contributed equally to this manuscript

Planets form in the disks around young stars. Their formation efficiency and composition are intimately linked to the protoplanetary disk locations of “snow lines” of abundant volatiles. We present chemical imaging of the CO snow line in the disk around TW Hya, an analog of the solar nebula, using high spatial and spectral resolution Atacama Large Millimeter/Submillimeter Array (ALMA) observations of N_2H^+ , a reactive ion present in large abundance only where CO is frozen out. The N_2H^+ emission is distributed in a large ring, with an inner radius that matches CO snow line model predictions. The extracted CO snow line radius of ~ 30 AU helps to assess models of the formation dynamics of the Solar System, when combined with measurements of the bulk composition of planets and comets.

Condensation fronts in protoplanetary disks, where abundant volatiles deplete out of the gas phase and are incorporated into solids, are believed to have played a critical role in the formation of planets in the Solar System (1, 2), and similar “snow lines” in the disks around young stars should affect the ongoing formation of exoplanets. Snow lines can enhance particle growth and thus planet formation efficiencies because of 1) substantial increases in solid mass surface densities exterior to snow line locations, 2) continuous freeze-out of gas diffusing across

the snow line (cold-head effect), 3) pile-up of dust just inside of the snow line in pressure traps, and 4) an increased stickiness of icy grains compared to bare ones, which favors dust coagulation (3–7). Experiments and theory on these processes have been focused on the H₂O snow line, but the results should be generally applicable to snow lines of abundant volatiles, with the exception that the “stickiness” of different icy grain mantles varies. The locations of snow lines of the most abundant volatiles – H₂O, CO₂, and CO – with respect to the planet-forming zone may also regulate the bulk composition of planets (8). Determining snow line locations is therefore key to probing grain growth, and thus planetesimal and planet formation efficiencies, and elemental and molecular compositions of planetesimals and planets forming in protoplanetary disks, including the solar nebula.

Based on the Solar System composition and disk theory, the H₂O snow line developed at ~ 3 Astronomical Units (AU, where 1 AU is the distance from the Earth to the Sun) from the early Sun during the epoch of chondrite assembly (9). In other protoplanetary disks the snow line locations are determined by the disk midplane temperature structures, set by a time dependent combination of the luminosity of the central star, the presence of other heating sources, the efficiencies of dust and gas cooling, and the intrinsic condensation temperatures of different volatiles. Because of the low condensation temperature of CO, the CO snow line occurs at radii of 10’s of AU around Solar-type stars: this larger size scale makes the CO transition zone the most accessible to direct observations. The CO snow line is also important in its own right, because CO ice is a starting point for a complex, prebiotic chemistry (10). Also without incorporating an enhanced grain growth efficiency beyond that expected for bare silicate dust, observations of centimeter sized dust grains in disks, including in TW Hya (11), are difficult to reproduce in the outer disk. Condensation of CO is very efficient below the CO freeze-out temperature, with a sticking efficiency close to unity based on experiments (12), and a CO condensation-based dust growth mode may thus be key to explaining these observations.

Protoplanetary disks have evolving radial and vertical temperature gradients, with a warmer surface where CO remains in the gaseous state throughout the disk, even as it is frozen in the cold, dense region beyond the midplane snow line (13). This means that the midplane snow line important for planet formation constitutes a smaller portion of a larger condensation surface. Because the bulk of the CO emission comes from the disk surface layers, this presents a challenge for locating the CO midplane snow line. Its location has been observationally identified toward only one system, the disk around HD 163296, based on (sub-)millimeter interferometric observations of multiple CO rotational transitions and isotopologues at high spatial resolution, interpreted through detailed modeling of the disk dust and gas physical structure (14). An alternative approach to constrain the CO snow line, suggested in (15) and pursued here, is to image molecular emission from a species that is abundant only where CO is highly depleted from the gas phase.

N₂H⁺ emission is expected to be a robust tracer of CO depletion because the presence of gas phase CO both slows down N₂H⁺ formation and speeds up N₂H⁺ destruction. N₂H⁺ forms through reactions between N₂ and H₃⁺, but most H₃⁺ will instead transfer a proton to CO as long as the more abundant CO remains in the gas phase. The most important destruction mech-

anism for N_2H^+ is proton transfer to a CO molecule, whereas in the absence of CO, N_2H^+ is destroyed through a much slower dissociative recombination reaction. These simple astrochemical considerations predict a correlation between N_2H^+ and CO depletion, or equivalently an anti-correlation between N_2H^+ and gas-phase CO. The latter has been observed in many pre-stellar and protostellar environments, confirming the basic theory (16, 17). In disks N_2H^+ should therefore be present at large abundances only inside the vertical and horizontal thermal layers where CO vapor is condensing, i.e., beyond the CO snow line. Molecular line surveys of disks have shown that N_2H^+ is only present in disks cold enough to entertain CO freeze-out (18), and marginally resolved observations hint at a N_2H^+ emission offset from the stellar position (15), in agreement with the models of disk chemistry (19). Detailed imaging of N_2H^+ emission in protoplanetary disks at the scales needed to directly reveal CO snow lines with sufficient sensitivity has previously been out of reach.

We used ALMA to obtain images of emission from the 372 GHz dust continuum and the N_2H^+ $J = 4 - 3$ line from the disk around TW Hya (Fig. 1, S1) (20). TW Hya is the closest (54 ± 6 pc) and as such the most intensively-studied pre-main-sequence star with a gas-rich circumstellar disk (21, 22). Based on previous observations of dust and CO emission, and the recent detection of HD line emission (23), this 3–10 million year old, $0.8 M_\odot$ T Tauri star (spectral type K7) is known to be surrounded by an almost face-on ($\sim 6^\circ$ inclination) massive $\sim 0.04 M_\odot$ gas-rich disk. The disk size in millimeter dust is ~ 60 AU, with a more extended (> 100 AU) disk in gas and micrometer-sized dust (24). Both the disk mass and size conforms well with solar nebula estimates – the minimum mass of the solar nebula is $0.01 M_\odot$ based on planet masses and compositions (9) – and the disk around TW Hya may thus serve as a template for planet formation in the solar nebula. Our images show that N_2H^+ emission is distributed in a ring with an inner diameter of 0.8 to 1.2 arcsec (based on visual inspection), corresponding to a physical inner radius of 21 to 32 AU. By contrast, CO emission is detected down to radial scales ~ 2 AU (25). The clear difference in morphology between the N_2H^+ and CO emission can be simply explained by the presence of a CO midplane snow line at the observed inner edge of the N_2H^+ emission ring. The different morphologies cannot be explained by a lack of ions in the inner disk based on previous spatially and spectrally resolved observations of another ion, HCO^+ (22). These HCO^+ observations had lower sensitivity and angular resolution than the N_2H^+ observations, but they are sufficient to exclude a central hole comparable in size to that seen in N_2H^+ .

To associate the inner edge radius of the N_2H^+ emission with a midplane temperature, and thus a CO freeze-out temperature, requires a model of the disk density and temperature structure. We adopted the model presented in (22), updated to conform with recent observations of the accretion rate and grain settling (Fig. S2–S4, Table S1) (20). In the context of this disk structure model, the N_2H^+ inner edge location implies that N_2H^+ becomes abundant where the midplane temperature drops to 16–20 K. This is in agreement with expectations for the CO freeze-out temperature based on the outcome of the laboratory experiments and desorption modeling by (12), who found CO condensation/sublimation temperatures of 16–18 K under interstellar conditions, assuming heat-up rates of 1 K per 10^2 to 10^6 years. In outer disk mid-

planes, condensation temperatures are expected to at most a few degrees higher because of a weak dependence on density (26). If CO condenses onto H₂O ice rather than existing CO ice, the condensation temperature will increase further, but this will only affect the first few monolayers of ice and is not expected to change the location where the majority of CO freezes out. Some CO may also remain in the gas phase below the CO freeze-out temperature in the presence of efficient non-thermal desorption, especially UV photodesorption (27), but this is expected to be negligible in the disk midplane at 30 AU, because of UV shielding by upper disk layers. UV photodesorption may affect the vertical CO snow surface location, however, and it may thus not be possible to describe the radial and vertical condensation surfaces by a single freeze-out temperature.

To locate the inner edge of the N₂H⁺ ring more quantitatively, we simulated the N₂H⁺ emission with a power-law column density distribution and compared with the data. We assumed the disk material orbits the central star in Keplerian motion, and fixed the geometric and kinematic parameters of the disk that affect its observed spatio-kinematic behavior (22). We used the same, updated density and temperature disk structure model (20), and assumed that the N₂H⁺ column density structure could be approximated as a radial power-law with inner and outer edges, while vertically the abundance was taken to be constant between the lower (toward midplane) and upper (toward surface) boundaries. This approach crudely mimics the results of detailed astrochemical modeling of disks, which shows that molecules are predominantly present in well-defined vertical layers (13, 19), and has been used to constrain molecular abundance structures in a number of previous studies (15, 22). The inner and outer radii, power-law index, and column density at 100 AU were treated as free parameters. We calculated a grid of synthetic N₂H⁺ visibility datasets using the RATRAN code (28) to determine the radiative transfer and molecular excitation, and compared with the N₂H⁺ observations. We obtained the best-fit model by minimizing χ^2 , the weighted difference between the data and the model with the real and imaginary part of the complex visibility measured in the (u, v) -plane sampled by the ALMA observations of N₂H⁺.

Fig. 2a demonstrates that the inner radius is well constrained to 28–31 AU (3σ). This edge determination was aided by the nearly face-on viewing geometry, because this minimizes the impact of the detailed vertical structure on the disk modeling outcome. Furthermore, the Keplerian kinematics of the gas help to constrain the size scale at a level finer than the spatial resolution implied by the synthesized beam size. As a result, the fitted inner radius is robust to the details of the density and temperature model (20) (Table S2). In the context of this model, the best-fit N₂H⁺ inner radius corresponds to a CO midplane snow line at a temperature of 17 K. Fig. 2b presents the best-fit N₂H⁺ column density profile together with the best-fit ¹³CO profile, assuming a CO freeze-out temperature of 17 K (20) (Fig. S5, Table S3). We fit ¹³CO emission (obtained with the Submillimeter Array (20)) because the main isotopologue CO lines are optically thick. The N₂H⁺ column density contrast across the CO snow line is at least an order of magnitude (20). Fig. 2c shows simulated ALMA observations of the best-fit N₂H⁺ $J = 4 - 3$ model, demonstrating the excellent agreement.

Our quantitative analysis thus confirms the predictions that N₂H⁺ traces the snow line of

the abundant volatile, CO. Furthermore, the agreement between the quantitative analysis and the visual estimate of the N_2H^+ inner radius demonstrate that N_2H^+ imaging is a powerful tool to determine the CO snow line radii in disks, whose density and temperature structures have not been modeled in detail. N_2H^+ imaging with ALMA may therefore be used to provide statistics on how snow line locations depend on parameters of interest for planet formation theory, such as the evolutionary stage of the disks.

The locations of snow lines in solar nebula analogs like TW Hya are also important to understand the formation dynamics of the Solar System. The H_2O snow line is key to the formation of Jupiter and Saturn (29), while CH_4 and CO freeze-out enhanced the solid surface density further out in the solar nebula, which may have contributed to the feeding zones of Uranus and Neptune (30), depending on exactly where these ice giants formed. In the popular Nice model for the dynamics of the young Solar System, Uranus formed at the largest radius of all planets, at ~ 17 AU (31), and most comets and Kuiper Belt objects formed further out, to ~ 35 AU. The plausibility of this scenario can be assessed using the bulk compositions of these bodies together with knowledge of the CO snow line location. In particular, Kuiper Belt objects contain CO and the even more volatile N_2 (32, 33), which implies that they must have formed beyond the CO snow line. Comets exhibit a range of CO abundances, some of which seem to be primordial, which suggest the CO snow line was located in the outer part of their formation region of 15–35 AU (34). This is consistent with the CO snow line radius that we have determined in the TW Hya disk. However, in the context of the Nice model, this CO snow line radius is too large for the ice giants, and suggests that their observed carbon enrichment has a different origin than the accretion of CO ice (30). A caveat is that H_2O ice can trap CO, though this process is unlikely to be efficient enough to explain the observations. In either case, the CO snow line locations in solar nebula analogs like TW Hya offers independent constraints on the early history of the Solar System.

References and Notes

1. J. S. Lewis, *Science* **186**, 440 (1974).
2. D. J. Stevenson, J. I. Lunine, *Icarus* **75**, 146 (1988).
3. F. J. Ciesla, J. N. Cuzzi, *Icarus* **181**, 178 (2006).
4. A. Johansen, *et al.*, *Nature* **448**, 1022 (2007).
5. E. Chiang, A. N. Youdin, *Annual Review of Earth and Planetary Sciences* **38**, 493 (2010).
6. B. Gundlach, S. Klias, E. Beitz, J. Blum, *Icarus* **214**, 717 (2011).
7. K. Ros, A. Johansen, *A&A* **552**, A137 (2013).
8. K. I. Öberg, R. Murray-Clay, E. A. Bergin, *ApJL* **743**, L16 (2011).

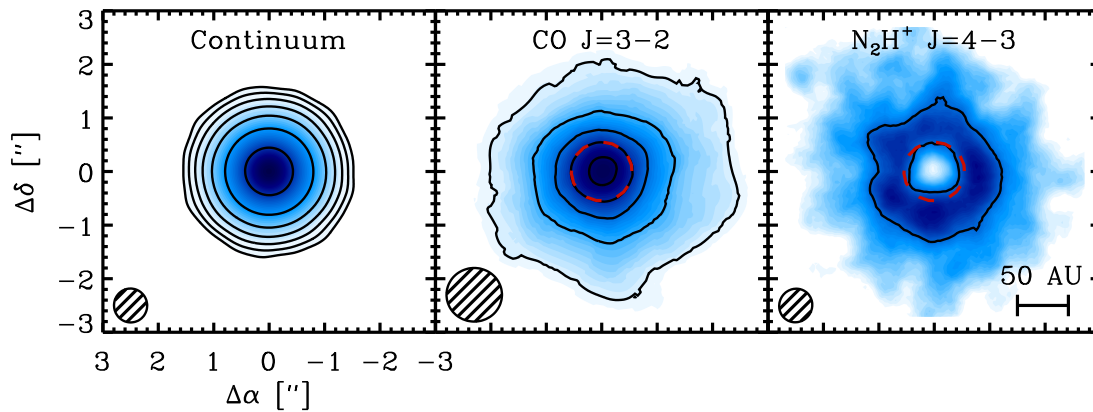


Fig. 1: Observed images of dust, CO and N_2H^+ emission toward TW Hya. *Left:* ALMA 372 GHz continuum map, extracted from the line free channels of the N_2H^+ observations. Contours mark [5, 10, 20, 40, 80, 160, 320] mJy beam^{-1} and the rms is $0.2 \text{ mJy beam}^{-1}$. *Center:* image of CO $J = 3 - 2$ emission acquired with the SMA (24). Contours mark [1, 2, 3, 4, 5] $\text{Jy km s}^{-1} \text{ beam}^{-1}$ and the rms is $0.1 \text{ Jy km s}^{-1} \text{ beam}^{-1}$. *Right:* ALMA image of N_2H^+ $J = 4 - 3$ integrated emission with a single contour at $150 \text{ mJy km s}^{-1} \text{ beam}^{-1}$ and the rms is $10 \text{ mJy km s}^{-1} \text{ beam}^{-1}$. The synthesized beam sizes are shown in the bottom left corner of each panel. The red dashed circle marks the best-fit inner radius of the N_2H^+ ring from a modeling of the visibilities. This inner edge traces the onset of CO freeze-out according to astrochemical theory, and thus marks the CO snow line in the disk midplane.

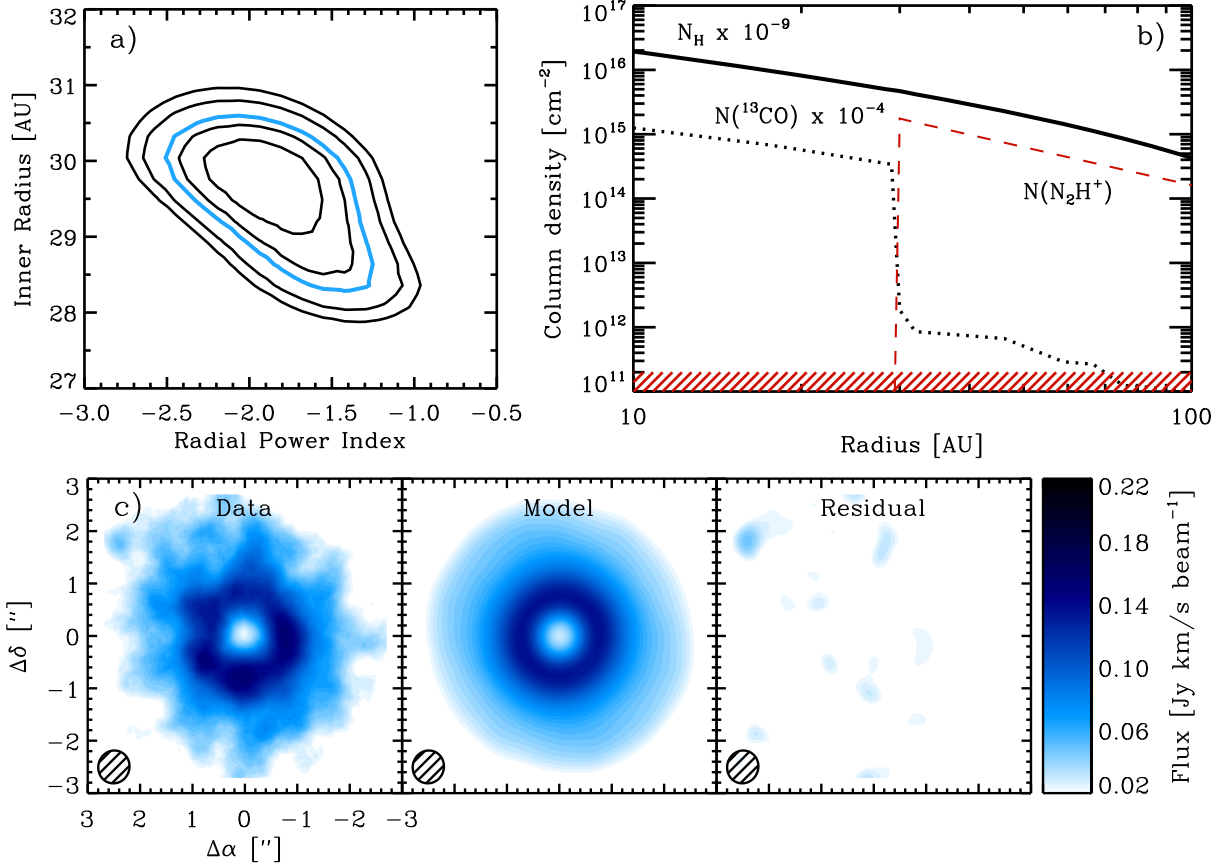


Fig. 2: Model results for the N_2H^+ abundance structure toward TW Hya. *Upper left:* The χ^2 fit surface for the power law index and inner radius of the N_2H^+ abundance profile. Contours correspond to the 1–5 σ errors and the blue contour marks 3σ . *Upper right:* The best fit N_2H^+ column density structure, shown together with the total gas column density and the best-fit ^{13}CO column density for CO freeze-out at 17 K. The shaded region marks the N_2H^+ 1σ detection limit. *Lower panel:* N_2H^+ observations, simulated observations of the best-fit N_2H^+ model, and the imaged residuals, calculated from the visibilities.

9. C. Hayashi, *Progress of Theoretical Physics Supplement* **70**, 35 (1981).
10. E. Herbst, E. F. van Dishoeck, *ARA&A* **47**, 427 (2009).
11. D. J. Wilner, P. D'Alessio, N. Calvet, M. J. Claussen, L. Hartmann, *ApJL* **626**, L109 (2005).
12. S. E. Bisschop, H. J. Fraser, K. I. Öberg, E. F. van Dishoeck, S. Schlemmer, *A&A* **449**, 1297 (2006).
13. Y. Aikawa, E. Herbst, *A&A* **351**, 233 (1999).
14. C. Qi, *et al.*, *ApJ* **740**, 84 (2011).
15. C. Qi, K. I. Öberg, D. J. Wilner, *ApJ* **765**, 34 (2013).
16. E. A. Bergin, J. Alves, T. Huard, C. J. Lada, *ApJL* **570**, L101 (2002).
17. J. K. Jørgensen, *A&A* **424**, 589 (2004).
18. K. I. Öberg, *et al.*, *ApJ* **734**, 98 (2011).
19. C. Walsh, H. Nomura, T. J. Millar, Y. Aikawa, *ApJ* **747**, 114 (2012).
20. Materials and methods are available as supporting material on Science Online.
21. J. H. Kastner, B. Zuckerman, D. A. Weintraub, T. Forveille, *Science* **277**, 67 (1997).
22. C. Qi, D. J. Wilner, Y. Aikawa, G. A. Blake, M. R. Hogerheijde, *ApJ* **681**, 1396 (2008).
23. E. A. Bergin, *et al.*, *Nature* **493**, 644 (2013).
24. S. M. Andrews, *et al.*, *ApJ* **744**, 162 (2012).
25. K. A. Rosenfeld, *et al.*, *ApJ* **757**, 129 (2012).
26. D. Hollenbach, M. J. Kaufman, E. A. Bergin, G. J. Melnick, *ApJ* **690**, 1497 (2009).
27. K. Willacy, *ApJ* **660**, 441 (2007).
28. M. R. Hogerheijde, F. F. S. van der Tak, *A&A* **362**, 697 (2000).
29. M. Lecar, M. Podolak, D. Sassellov, E. Chiang, *ApJ* **640**, 1115 (2006).
30. S. E. Dodson-Robinson, K. Willacy, P. Bodenheimer, N. J. Turner, C. A. Beichman, *Icarus* **200**, 672 (2009).
31. K. Tsiganis, R. Gomes, A. Morbidelli, H. F. Levison, *Nature* **435**, 459 (2005).
32. T. C. Owen, *et al.*, *Science* **261**, 745 (1993).

33. S. C. Tegler, *et al.*, *ApJ* **751**, 76 (2012).
34. M. J. Mumma, S. B. Charnley, *ARA&A* **49**, 471 (2011).
35. P. D'Alessio, J. Canto, N. Calvet, S. Lizano, *ApJ* **500**, 411 (1998).
36. P. D'Alessio, N. Calvet, L. Hartmann, S. Lizano, J. Cantó, *ApJ* **527**, 893 (1999).
37. P. D'Alessio, N. Calvet, L. Hartmann, *ApJ* **553**, 321 (2001).
38. P. D'Alessio, N. Calvet, L. Hartmann, R. Franco-Hernández, H. Servín, *ApJ* **638**, 314 (2006).
39. N. I. Shakura, R. A. Sunyaev, *MNRAS* **175**, 613 (1976).
40. N. Calvet, *et al.*, *ApJL* **630**, L185 (2005).
41. C. Espaillat, *et al.*, *ApJL* **670**, L135 (2007).
42. C. Espaillat, *et al.*, *ApJ* **717**, 441 (2010).
43. L. Hartmann, N. Calvet, E. Gullbring, P. D'Alessio, *ApJ* **495**, 385 (1998).
44. A. M. Hughes, D. J. Wilner, C. Qi, M. R. Hogerheijde, *ApJ* **678**, 1119 (2008).
45. N. Calvet, *et al.*, *ApJ* **568**, 1008 (2002).
46. K. I. Uchida, *et al.*, *ApJS* **154**, 439 (2004).
47. A. M. Hughes, D. J. Wilner, S. M. Andrews, C. Qi, M. R. Hogerheijde, *ApJ* **727**, 85 (2011).
48. G. J. Herczeg, B. E. Wood, J. L. Linsky, J. A. Valenti, C. M. Johns-Krull, *ApJ* **607**, 369 (2004).
49. F. L. Schöier, F. F. S. van der Tak, E. F. van Dishoeck, J. H. Black, *A&A* **432**, 369 (2005).
50. P. T. P. Ho, J. M. Moran, K. Y. Lo, *ApJL* **616**, L1 (2004).
51. C. Qi, *et al.*, *ApJL* **636**, L157 (2006).
52. C. Qi, *et al.*, *ApJL* **616**, L11 (2004).

Acknowledgments

We are grateful to S. Schnee for data calibration and reduction assistance. C.Q. would like to thank the SAO Radio Telescope Data Center (RTDC) staff for their generous computational support. C.Q., K.I.O. and D.J.W. acknowledges a grant from NASA Origins of Solar Systems grant No. NNX11AK63. P.D. acknowledges a grant from PAPIIT-UNAM. E.A.B. acknowledges support from NSF Grant#1008800. This Report makes use of the following ALMA data:

ADSJAO.ALMA#2011.0.00340.S. ALMA is a partnership of ESO (representing its member states), NSF (USA), and NINS (Japan), together with NRC (Canada) and NSC and ASIAA (Taiwan), in cooperation with the Republic of Chile. The Joint ALMA Observatory is operated by ESO, AUI/NRAO, and NAOJ. We also make use of the Submillimeter Array (SMA) data: project #2004-214 (PI: C. Qi). The SMA is a joint project between the Smithsonian Astrophysical Observatory and the Academia Sinica Institute of Astronomy and Astrophysics and is funded by the Smithsonian Institution and the Academia Sinica.

Supporting Online Material

www.sciencemag.org/cgi/content/full/science.1239560/DC1

Materials and Methods

Table S1–S3

Figs S1–S5

References (35–52)

Materials and Methods

Observational details

Continuum and N_2H^+ line observations toward TW Hya were carried out in ALMA band 7 (PI: C. Qi) on 19 November, 2012, with 23 to 26 antennas in the Cycle 0 compact configuration. The correlator was configured to observe four windows with a channel spacing of $\delta\nu = 61.04$ kHz and a bandwidth of 234.375 MHz each. The windows were centered at 372.672 GHz (SPW#1), the rest frequency of the N_2H^+ $J = 4 - 3$ line, 372.421 GHz (SPW#0), 358.606 GHz (SPW#2), and 357.892 GHz (SPW#3). The nearby quasar J1037-295 was used for phase and gain calibration and 3C279 and J0522-364 were used as bandpass calibrators. The primary calibrator Ceres provided a mean flux density of 0.61 Jy for the gain calibrator J1037-295. The visibility data were reduced and calibrated in CASA 3.4.

The atmospheric transmission in the upper (372 GHz) and lower (358 GHz) sidebands is very different due to strong absorption near 370 GHz. Therefore, we reduced the data separately for both sidebands. The continuum visibilities were extracted by averaging the line-free channels in SPW# 0, 1 (upper sideband) and 2,3 (lower sideband), respectively. We carried out self-calibration procedures on the continuum as demonstrated in the TW Hya Science Verification Band 7 CASA Guides, which are available online (<https://almascience.nrao.edu/alma-data/science-verification/tw-hya>). The synthesized beam and RMS for the continuum maps are $0.''63 \times 0.''60$ ($PA = 3^\circ$), $0.61 \text{ mJy beam}^{-1}$ (upper sideband) and $0.''57 \times 0.''55$ ($PA = 17^\circ$), $0.24 \text{ mJy beam}^{-1}$ (lower sideband). The continuum peak flux densities are determined to be 2.0097 ± 0.0062 Jy at 372 GHz and 1.7814 ± 0.0044 Jy at 358 GHz, which agrees with previous SMA observations and ALMA science verification data (24, 25). We applied the upper sideband continuum self-calibration correction to the N_2H^+ $J = 4 - 3$ line data and subtracted the continuum emission in the visibility domain.

The resulting synthesized beam for the N_2H^+ $J = 4 - 3$ data cube is $0.''63 \times 0.''59$ ($PA = -18^\circ$), and the 1σ rms is 30 mJy beam^{-1} in 0.1 km s^{-1} velocity intervals or $8.1 \text{ mJy beam}^{-1} \text{ km s}^{-1}$, which corresponds to a column density detection limit of $2 \times 10^{11} \text{ cm}^{-2}$ at 17 K. Fig. S1 shows the resulting channel maps for N_2H^+ $J = 4 - 3$.

Physical model

The physical model used to interpret the ALMA observations is a steady viscous accretion disk, heated by irradiation from the central star and mechanical energy generated by viscous dissipation near the disk midplane (35–38). The disk model is axisymmetric, in vertical hydrostatic equilibrium, and the viscosity follows the α prescription (39). Energy is transported in the disk by radiation, convection (in regions where the Schwarzschild stability criterion is not satisfied) and a turbulent energy flux. The penetration of the stellar and shock generated radiation is calculated using the two first moments of the radiative transfer equation, taking into account scattering and absorption by dust grains. This model framework has been used to successfully re-

produce observed disk structures towards several T Tauri and Herbig Ae stars (11, 14, 22, 40–42). Following (14, 43, 44), the model includes a tapered exponential edge to simulate viscous spreading: $\Sigma \sim \dot{M}\Omega_k/\alpha T_c$, with $\alpha(R) = \alpha_0 \exp(-R/R_c)$. Using the parameter values listed in Table S1, this physical model provides a good fit to the broadband spectral energy distribution (SED) of the disk of TW Hya (Fig. S2), except for the mid- and far-IR wavelengths, which is complicated by contributions of the inner disk wall, around 3.5–4 AU and optically thin hot dust from the inner hole, according to (45, 46). The α_0 adopted in this model is also consistent with the upper limit on the turbulent line widths, ($< 40 \text{ m s}^{-1}$) at ~ 1 – 2 scale heights (47), and an ever lower turbulence is expected in the midplane.

Following (14), given a measured disk mass accretion rate, $2 \times 10^{-9} M_\odot \text{ yr}^{-1}$ (48), and the viscous α parameter as formulated above, the vertical temperature and density structures are mainly regulated by the degree of grain growth and settling. In the present model, we introduce this effect in a parametric way. The dust is assumed to consist of two populations of grains with different size distribution functions (38), with $a_{max}^{small} = 0.25 \mu\text{m}$ (as in the interstellar medium) and $a_{max}^{big} = 1 \text{ mm}$ (consistent with the SED slope at mm wavelengths), and different spatial distributions such that the abundance of the large grains increases towards the midplane. The small dust grain to gas mass ratio is parameterized by ζ_{small} , which is lower than the ISM value because a large fraction of the dust mass is contained in larger grains. The amount of dust that is in small dust grains is parameterized by $\epsilon = \zeta_{small}/\zeta_{ISM} < 1$. The amount of large dust grains (parameterized by ϵ_{big}) is calculated so that the total dust mass at each radius is conserved, and ϵ is constrained by the slope of the SED in the far-IR and sub-mm wavelength range. The maximum grain size in the model is set to 1 mm, despite observational evidence for the existence of cm-sized grains (11), because we found a power-law size distribution of grains with a maximum size in cm could not fit the mm SED slope. This is probably caused by a radial distribution difference for the mm and cm-sized dust grains due to differential dust migration. The exclusion of cm-sized grains should have no effect on the conclusions of this study since their impact on the midplane temperature structure is minimal.

The surface that separates the regions where the small and large dust grain populations dominate is parameterized by $z_{big}(R)$ in terms of the local gas scale heights, H . Different z_{big} values are expected to result in disk structures with different thermal profiles because of changes in the shape of the irradiation surface, which determines the fraction of stellar emission intercepted and reprocessed by the disk. We vary z_{big} between $2H$ and $3.5H$, which results in the different vertical disk temperature structures seen in Fig. S3. Around the observed inner edge of the N_2H^+ ring, changing z_{big} also changes the midplane temperature by up to 2 K (Fig. S4). Despite the importance of z_{big} for vertical temperature and density structure, Fig. S2 shows that models with different z_{big} values present small variations in the SEDs, and all models fit the observed SED satisfactorily. This is generally true for SED modeling because of the degeneracy of the dust data with the parameter z_{big} (14) and the nearly face-on disk geometry makes SED modeling especially challenging. The details of the vertical structure in the TW Hya disk are therefore uncertain, and below we analyze the N_2H^+ line emission using the full range of z_{big} values to explore its effect on our conclusions.

N₂H⁺ line modeling

We adopted the molecular abundance model introduced by (14, 22), and assumed that the N₂H⁺ emission originates in a vertical layer with a constant abundance between the surface (σ_s) and midplane (σ_m) boundaries which are represented by vertically integrated hydrogen column densities measured from the disk surface in units of $1.59 \times 10^{21} \text{ cm}^{-2}$. We fix the vertical surface boundary σ_s to 3.2 and the midplane boundary σ_m to 100, which simulates an emission layer close to the midplane, in accordance with model predictions. Fitting these boundaries would require a combination of a well constrained vertical temperature structure and multiple N₂H⁺ transitions and is thus outside of the scope of this study. To test the importance of the assumed vertical structure on the inferred radial distribution of N₂H⁺ we simulate N₂H⁺ visibilities for disk structure models with the range of z_{big} values and disk structures shown in Figs. S2-S4.

We model the radial distribution of N₂H⁺ as a power law $N_{100} \times (r/100)^p$ with an inner radius R_{in} and outer radius R_{out} , where N_{100} is the column density at 100 AU in cm^{-2} , r is the distance from the star in AU, and p is the power-law index. For each z_{big} structure model, we compute a grid of synthetic N₂H⁺ $J = 4 - 3$ visibility datasets over a range of R_{out} , R_{in} , p and N_{100} values and compare with the observations. The best-fit model is obtained by minimizing χ^2 , the weighted difference between the data and the model with the real and imaginary part of the complex visibility measured in the (u, v) -plane sampled by the ALMA observations. We use the two-dimensional Monte Carlo model RATRAN (28) to calculate the radiative transfer and molecular excitation. The collisional rate coefficients are taken from the Leiden Atomic and Molecular Database (49).

Table S2 gives the best-fit N₂H⁺ distribution parameters for each z_{big} model, as well as the corresponding midplane temperature T_c at the N₂H⁺ inner edge. The power law index of the surface density varies between 2.4 and -3.6 , and the column density at the inner edge between 4×10^{12} and $2 \times 10^{15} \text{ cm}^{-2}$. Given the 1σ detection limit of $2 \times 10^{11} \text{ cm}^{-2}$, the column density contrast at the inner edge of the N₂H⁺ ring is at least 20 and could be much larger. Across this range of models, the inner radius varies by less than 5 AU, and the midplane temperature at the inner radius varies by less than 1 K. The inner radius is thus well constrained, which implies that the key feature of the N₂H⁺ distribution needed to constrain the CO snow line is robust with respect to the details of the physical model assumptions. Channel maps for the best-fit model using the fiducial $z_{\text{big}} = 3H$ are shown in Fig. S1 together with the observed data and imaged residuals, demonstrating the excellent agreement.

CO distribution

To derive the CO distribution and test the self-consistency of the fiducial best-fit model, we also modeled two CO isotopologues which we observed with the Submillimeter Array (SMA) (50) in 2005 February 27 and April 10. The main isotopologue was also observed, but is optically thick and therefore not included in this analysis. The SMA receivers operated in a double-sideband mode with an intermediate frequency (IF) band of 4–6 GHz from the local oscillator

frequency, sent over fiber optic transmission lines to 24 overlapping “chunks” of the digital correlator. The correlator was configured to include CO, ^{13}CO and $\text{C}^{18}\text{O } J = 2 - 1$ in one setting: the tuning was centered on the CO $J = 2 - 1$ line at 230.538 GHz in chunk S15, while the $^{13}\text{CO } J = 2 - 1$ at 220.399 GHz and $\text{C}^{18}\text{O } J = 2 - 1$ at 219.560 GHz were simultaneously observed in chunk 12 and 22, respectively (51). Combinations of two array configuration (compact and extended) were used to obtain projected baselines ranging from 6 to 180 m. The observing loops used J1037-295 as the gain calibrator. The bandpass response was calibrated using observations of 3C279. Flux calibration was done using observations of Titan and Callisto. Routine calibration tasks were performed using the MIR software package (<http://www.cfa.harvard.edu/~cqi/mircook.html>), and imaging and deconvolution were accomplished in MIRIAD. The integrated fluxes are reported in Table S3. Fig. S5 shows the spatially integrated spectra of ^{13}CO and $\text{C}^{18}\text{O } J = 2 - 1$ extracted from the SMA channel maps in $8''$ square boxes centered on TW Hya.

Following (14), CO is assumed to be present in the disk between a lower boundary set by the CO freeze-out temperature derived from the N_2H^+ modeling, and an upper boundary set by photodissociation, though the choice of upper boundary in this case has a very small effect on the modeled emission profiles of ^{13}CO and C^{18}O . The CO abundance structure was optimized using the same procedure as for N_2H^+ above. Fig. S5 shows that the best-fit CO abundance distribution fits the CO isotopologue observations well when using the fiducial disk structure and assuming standard isotope ratios and CO freeze-out at the N_2H^+ inner edge temperature of 17 K. In contrast the models with much smaller z_{big} cannot reproduce the relative C^{18}O and ^{13}CO fluxes without order of magnitude deviations from the cosmic isotope ratios. More data with better sensitivity and resolution from the emission of CO and its isotopologues and a detailed surface heating model (as suggested by (51)) are needed to constrain the temperature structure and the z_{big} value in the disk of TW Hya.

Table S1: Physical model for the disk of TW Hya

Parameters	Values
Stellar and accretion properties	
Spectral type	K7
Effective temperature: T_* (K)	4110
Estimated distance: d (pc)	54
Stellar radius: R_* (R_\odot)	1.04
Stellar mass: M_* (M_\odot)	0.8
Accretion rate: \dot{M} ($M_\odot \text{ yr}^{-1}$)	2×10^{-9}
Disk structure properties	
Disk mass: M_d (M_\odot)	0.04
Characteristic radius: R_c (AU)	60
Viscosity coefficient: α_0	0.0007
Depletion factor of the atmospheric small grains: ϵ^a	0.01
z_{big}^a (H^b)	3.0
Disk geometric and kinematic properties ^c	
Inclination: i (deg)	6
Systemic velocity: V_{LSR} (km s^{-1})	2.86
Turbulent line width: δv_{turb} (km s^{-1})	0.05
Position angle: $P.A.$ (deg)	155

^aSee definition in paper.

^bGas scale height.

^cParameters adopted from (22, 24, 51, 52).

Table S2: N_2H^+ $J = 4 - 3$ fitting results^a

$z_{\text{big}} (H)$	R_{in} (AU)	T_c^b (K)	p	N_{100} (cm^{-2})	R_{out} (AU)
2.0	25_{-6}^{+4}	15–18	$2.4_{-0.3}^{+0.6}$	$(1.4 \pm 0.2) \times 10^{14}$	150 ± 10
2.5	30_{-3}^{+1}	15–16	$0.4_{-0.4}^{+0.6}$	$(2.9 \pm 0.5) \times 10^{14}$	140 ± 10
3.0	30_{-2}^{+1}	16–17	$-2.0_{-0.7}^{+0.5}$	$(1.6 \pm 0.3) \times 10^{14}$	140 ± 10
3.5	30_{-4}^{+1}	16–18	$-3.6_{-0.8}^{+0.6}$	$(2.5 \pm 0.4) \times 10^{13}$	140 ± 10

^aErrors within 3σ .

^bTemperature range based on Fig. S4.

Table S3: TW Hya CO isotopologue observation results.

Transition	Frequency (GHz)	Beam / <i>P.A.</i>	$\int F dv$ (Jy km s ⁻¹)
¹³ CO <i>J</i> = 2 – 1	220.399	2.''7 × 1.''8 / –3.0°	2.72[0.18]
C ¹⁸ O <i>J</i> = 2 – 1	219.560	2.''8 × 1.''9 / –1.3°	0.68[0.18]

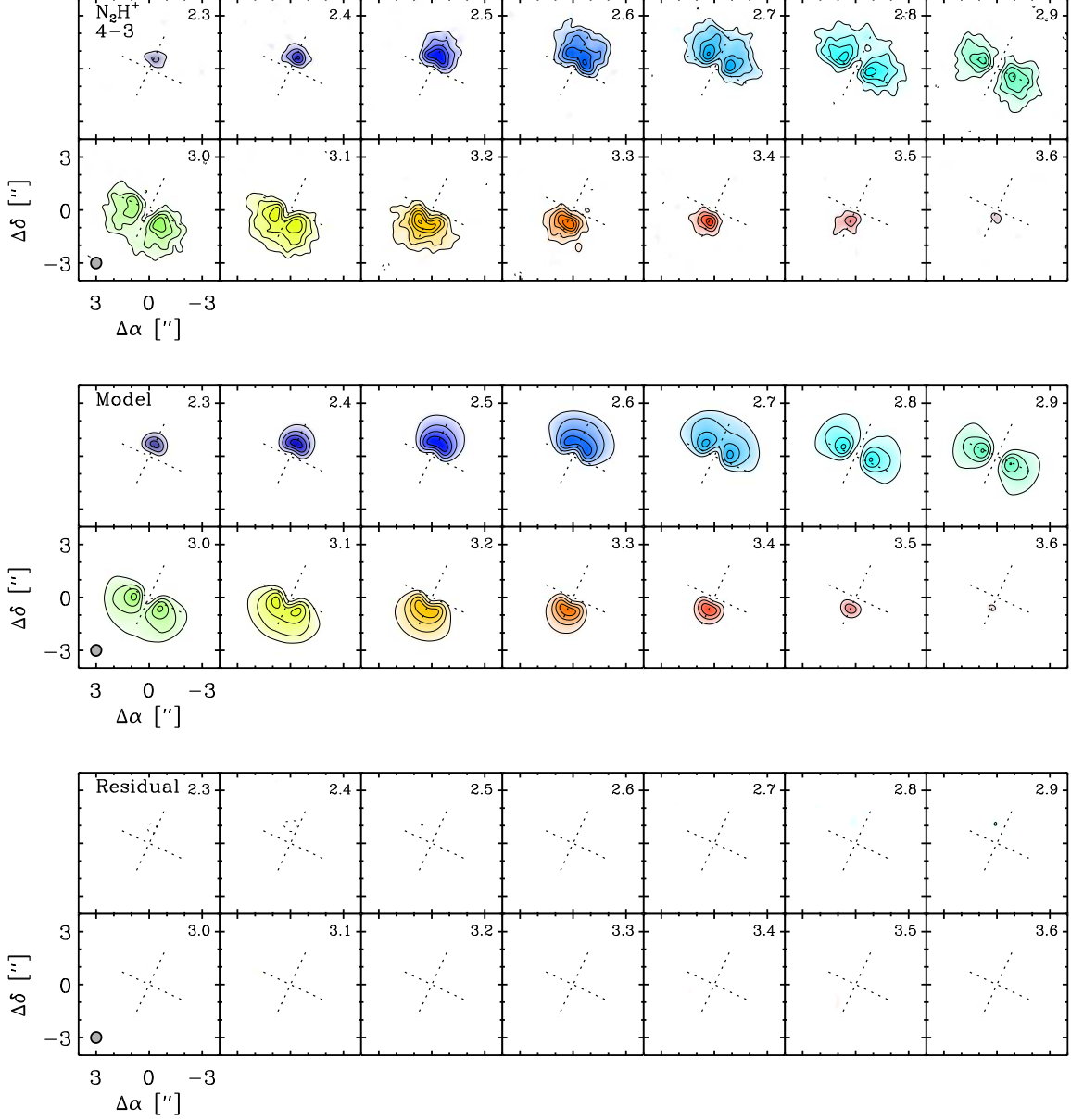


Fig. S1: Channel maps of the N_2H^+ $J = 4 - 3$ line emission observed by ALMA from the disk around TW Hya. The LSR velocity is indicated in the upper right of each channel, while the synthesized beam size and orientation ($0.''63 \times 0.''59$ at a position angle of -18.1°) is indicated in the lower left panel. The contours are $0.03 (1\sigma) \times [3, 6, 9, 12, 15, 18] \text{ Jy beam}^{-1}$.

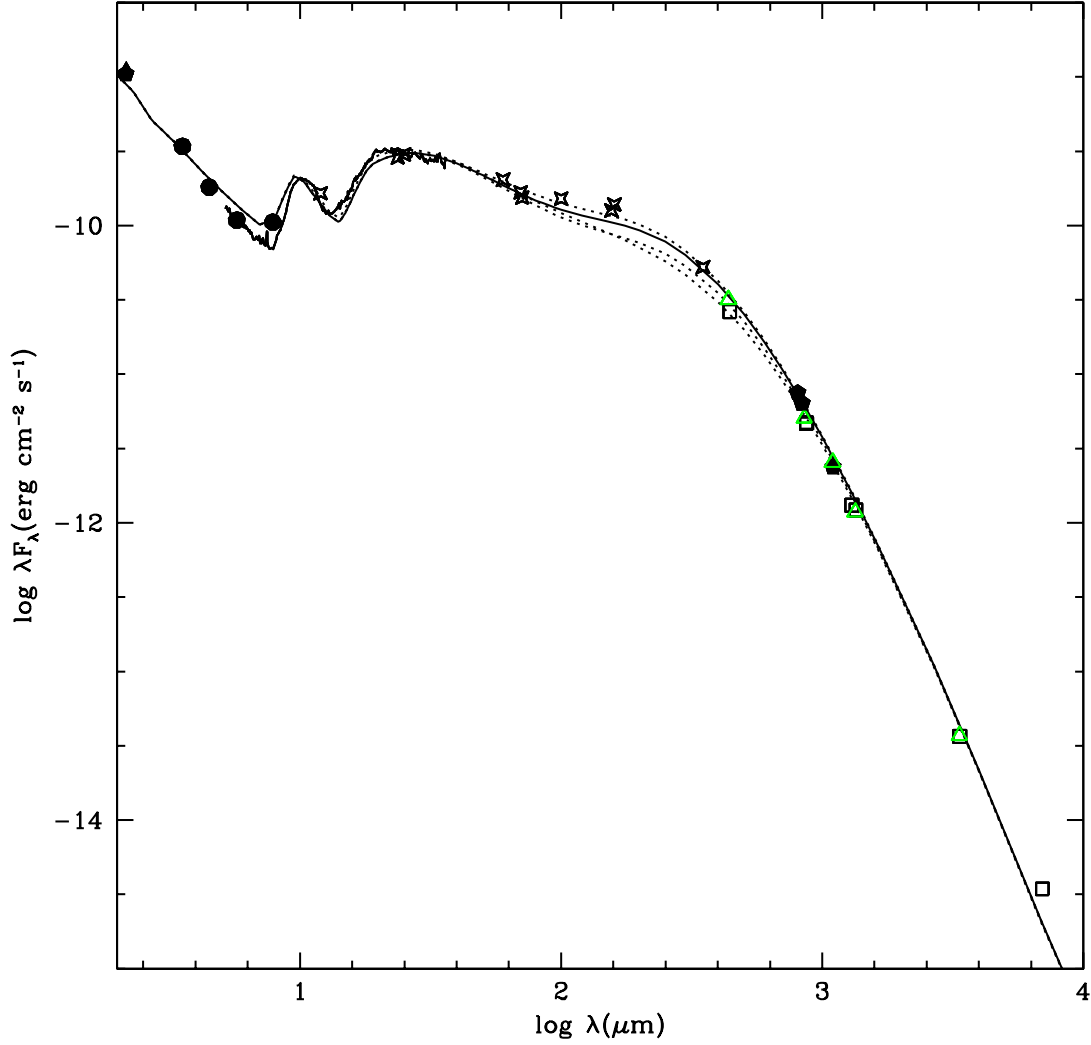


Fig. S2: The TW Hya SED and the model results for $\dot{M} = 2 \times 10^{-9} M_{\odot}/yr$, $\alpha_0 = 0.0007$, $\epsilon = 0.01$, and $R_c = 60$ AU. See the SED references in (24). The new mm/submm fluxes are from the ALMA science verification data and this paper (marked by green triangles). The different model SED lines correspond to $z_{\text{big}}/H = 2 - 3.5$, with the fiducial 3H model shown with a solid line, demonstrating that the SED modeling does not provide strong constraints on this parameter.

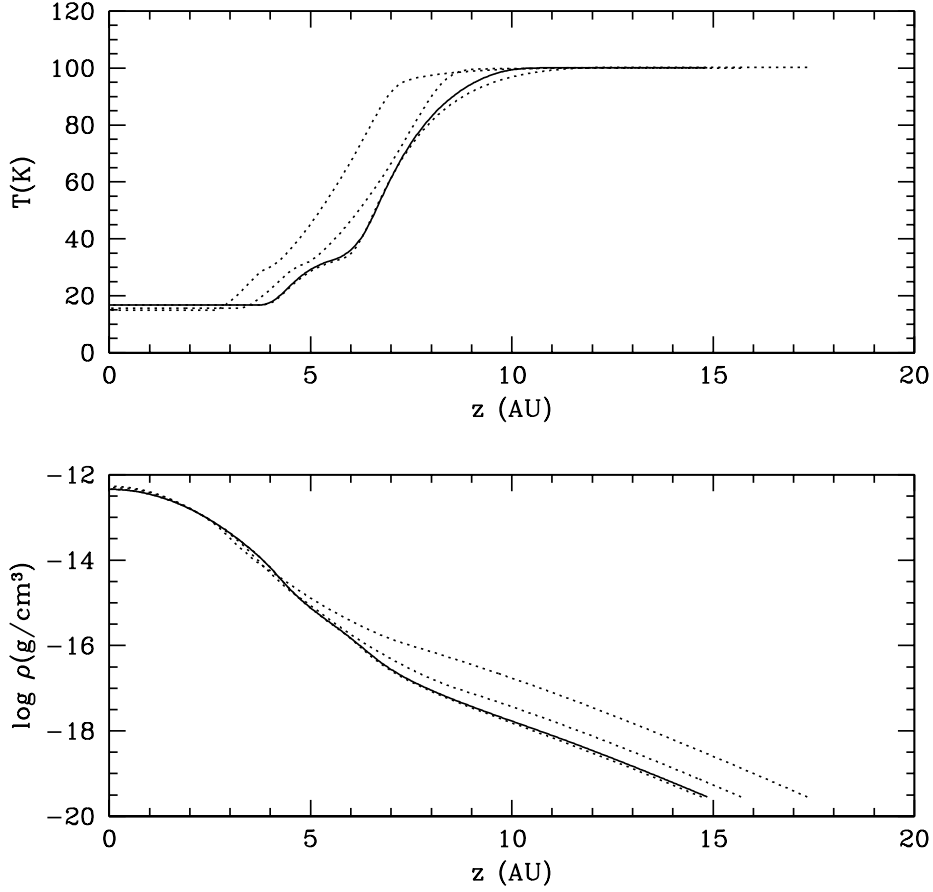


Fig. S3: Vertical temperature and density profiles at $R = 30$ AU for disk models with $\dot{M} = 2 \times 10^{-9} M_{\odot}/\text{yr}$, $\alpha_0 = 0.0007$, $\epsilon = 0.01$, $R_c = 60$ AU, and different values of z_{big} values. *Upper panel:* Temperature versus height at $R = 30$ AU for disk models with different values of $z_{\text{big}}/H = 2.0, 2.5, 3.0, 3.5$ (from left to right). The fiducial model, with $z_{\text{big}} = 3H$ is shown with a solid line. *Lower panel:* Density versus height at $R = 30$ AU for the same models. The lines from top to bottom correspond to models with $z_{\text{big}}/H = 2.0, 2.5, 3.0, 3.5$.

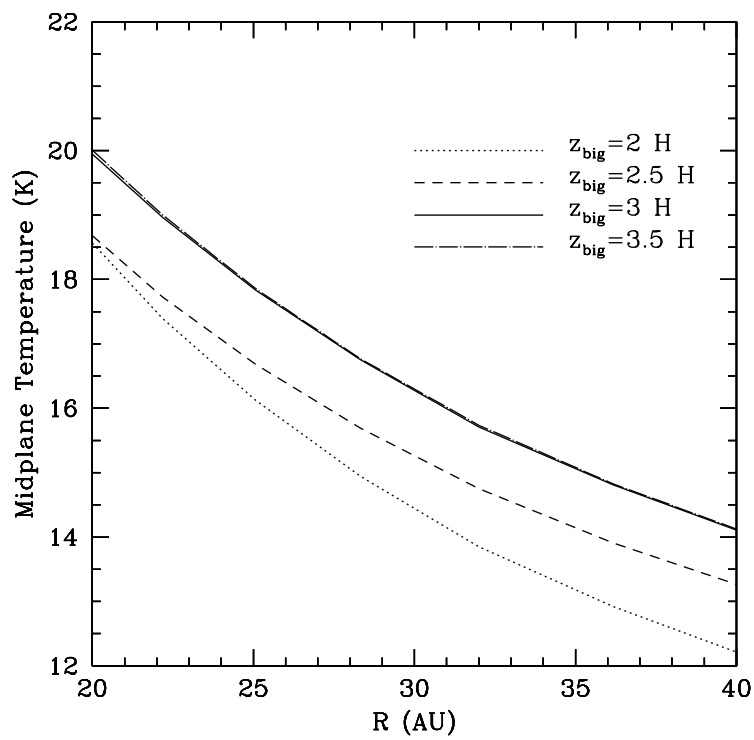


Fig. S4: Midplane temperature profiles for the TW Hya disk for different z_{big} values showing the effect of z_{big} on the midplane temperature around the N_2H^+ inner edge.

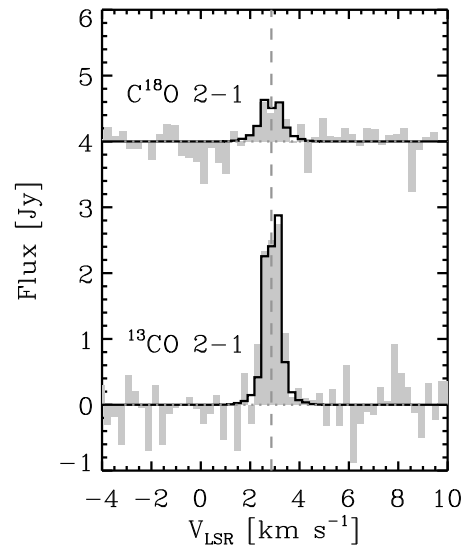


Fig. S5: CO isotopologue lines toward TW Hya, observed with the SMA (grey) and the best-fit CO modeling results using the fiducial disk structure developed to interpret the N_2H^+ observations. The dashed line marks the V_{LSR} toward TW Hya.